actuators

MDPI

Article

Design and Fabrication Method of a Soft Pneumatic Silicone Exosuit for Elbow Rehabilitation Assistance

Zhirui Zhao [1,*], Dequan Deng [1], Xinyu Hou [1], Chun Xia [1], Xinyu Zeng [1], Dexing Shan [1], Lina Hao [2] and Huicong Gao [3]

1 College of Mechatronics Engineering, Shenyang Aerospace University, Shenyang 110136, China
2 College of Mechanical and Electronic Engineering, Northeastern University, Shenyang 110819, China
3 College of Artificial Intelligence, Shenyang Aerospace University, Shenyang 110136, China
* Correspondence: 20220068@sau.edu.cn

Abstract

This study introduces the design process and fabrication method of a soft pneumatic silicone-based exosuit intended to assist human elbow extension and flexion movement for rehabilitation. First of all, an integrated fabrication method is developed to replace the step-by-step casting and cloth fiber layer, using a 3D-printed PVA mold in silicone casting to ensure the airtightness of the silicone actuator, and a carbon fiber woven mesh is used as the base plate of the actuator to improve its bending performance. Then, the finite element analysis is used to optimize the geometric parameters, hardness, and the number of air chambers for the exosuit structure. The experimental evaluation confirms that the exosuit achieves a bending angle of 112 degrees without any load and 71 degrees with a load of 2 kg. Combining with the PI angular controller, the system limits the maximum absolute tracking error to 4.29 degrees. These results also suggest the proposed exosuit is a promising candidate for practical rehabilitation tasks.

Keywords: soft exosuit; pneumatic actuator; finite element analysis; 3D-printed fabrication

Academic Editors: Lorenzo Bonetti, Giulia Scalet, Silvia Farè and Nicola Ferro

Received: 13 May 2026
Revised: 11 June 2026
Accepted: 16 June 2026
Published: 18 June 2026

1. Introduction

In contemporary society, every country faces a challenge in elderly healthcare, driven by aging populations and rising chronic diseases. Stroke, as a leading cause of physical disability, often severely impairs motor functions and reduces quality of life, intensifying the need for specialized rehabilitation services [1–3]. But the supply of rehabilitation physicians remains low, both in China and across 35 high-income countries, where the demand-to-supply ratio can exceed 40:1 [4,5]. This shortage calls for technological solutions, and robotic-assisted rehabilitation is a promising approach to enhance treatment efficiency and ensure sustainable healthcare delivery.

In the field of robot-assisted rehabilitation, the exoskeletons play a unique role among other robotic devices, which are designed to assist individuals with neurological and musculoskeletal disorders [1]. To reduce the reliance on rehabilitation physicians, these robots enable patients to engage in adjustable passive and active rehabilitation training tasks, preserve their functional independence in daily life, and even overcome their physical limitations in real-world scenarios [6–8]. Considering the case of the upper-limb exoskeleton, the typical conventional exoskeletons are constructed with several rigid links as the mechanical frame, which mimic the human arm, and are actuated by motors, pneumatic systems, and smart materials (e.g., SMA springs and pneumatic artificial muscles) combined with the artificial intelligence system [9–16]. Taking an example, ANYexo 2.0 is a neurological rehabilitation exoskeleton covering all relevant degrees of freedom of the human arm, providing enough range of motion, speed, and strength for rehabilitation therapy of severely affected and mildly affected patients, while its virtual haptic control method to enable safe, collision-free interaction with the human body [14]. Another representative and clinically validated exemplar is the ArmeoPower exoskeleton driven by DC motors, which has achieved widespread adoption in rehabilitation centers globally [16]. It employs a rigid multi-joint architecture, integrates active gravity compensation and impedance control algorithms, and utilizes game-like virtual reality (VR) training technology to assist patients in repetitive, task-specific motor training.

Nonetheless, the above-mentioned upper-limb exoskeleton robots belong to the rigid exoskeleton category due to their rigid material (such as carbon fiber and alloy) arm structure with a multi-link mechanism [17]. Despite their advantages in precise control performance, technological maturity, and arm support, rigid exoskeletons present several challenges for rehabilitation applications, including excessive weight and axis misalignment due to the industrial manipulate-inspired structural designs with high degrees of freedom, as well as bulkiness and high inertia that compromise user experience and training effectiveness [18]. Meanwhile, the repeated mechanical contact between the rigid material and the human arm may cause discomfort. To address the above issues, soft exoskeletons and exosuits have been designed, utilizing flexible actuators and compliant structures with wearable cloth materials to integrate seamlessly with the human body, providing targeted joint support and enhancing endurance without restricting natural movement [17–22]. For instance, Ismail and Li design a soft elbow exosuit by integrating fabric with 3D-printed connectors as the wearable interface, while employing cables and motor–tendon systems as the actuators, adhering to a bioinspired structural design with tensile wires that can mimic human muscle control principles [19,20]. Although these exosuits deliver assistive forces and reduce muscle activity during rehabilitation, they are limited by the fact that the motor–tendon systems inherently exhibit high tensile stiffness and pre-tensioning requirements from the cables, leading to local stress concentration during bending or external loading. Additional concerns include cable friction, wear, hysteresis effects, and complex installation procedures.

On the other hand, the soft pneumatic silicone exosuit also gives a change to bypass the multi-link mechanism and rigid structure in the robotic systems [22,23]. To our best knowledge, silicone offers excellent moldability, airtightness, and enables diverse structural designs that conform to the upper-limb and hand morphology [24]. Meanwhile, owing to its supreme plasticity, bio-compatibility, and fast prototyping capability, the silicone material is widely employed in actuation structures, grasping mechanisms and bionic robots, where ingenious design of air chambers enables bending and stretching movements to be readily achieved [25–28]. For instance, Gao designed a soft pneumatic elbow pad (SPEP) with a unique air chamber structure, integrated sensors, and a portable backpack system to assist elbow flexion and extension and reduce muscle activity [17]. Sridhar designs a pneumatic elbow exoskeleton (PASE) for people in different rehabilitation training tasks. It also used silicone as an actuator and combines 3D printing materials with chloroprene rubber as a contact surface [28]. Despite progress, soft pneumatic silicone exosuits remain a technically demanding area of research. Relevant researchers often rely on trial-and-error approaches and their own experience, without systematic analysis of silicone nonlinearities or structural parameters via finite element simulation, leading to lengthy design cycles and suboptimal performance. Furthermore, for most silicone pneumatic robots, air chambers are typically fabricated by casting using multi-piece split molds, which can be assembled to form the

https://doi.org/10.3390/act15060348

cavity into which elastic materials such as silicone rubber are then injected. However, this approach suffers from the following major drawbacks: First of all, during assembly, micro-gaps and misalignments inevitably occur between the contact surfaces of the multiple mold parts, compromising the molding precision of the air chambers and the uniformity of wall thickness. Second, the demolding process often causes hidden damage, such as scratches or tears, in thin-walled regions of the chambers, reducing the consistency of the final products. These defects easily induce local stress concentrations, cracking, and even air leakage under subsequent pressurization, severely impairing the service life.

Some scholars have attempted to improve the airtightness of silicone layers by adopting multiple-piece mold casting combined with an inter-adhesion process of V-groove structures on silicone surfaces or fabric structures with other soft materials (e.g., TPU) [29,30]. However, this approach increases the complexity of mold design and the demolding process. In contrast, other researchers have employed integrated casting methods, in which the inner mold can change its physical state under different conditions (e.g., temperature), as demonstrated by lost-wax casting and water-soluble mold methods [31,32]. For instance, lost-wax casting uses a wax core that is melted away, while water-soluble mold methods employ 3D-printed PVA as a sacrificial core that can be dissolved. These integrated approaches eliminate the need for multi-piece assembly and reduce demolding-related damage, but they also require careful design of cavity structures to ensure complete removal of the sacrificial material. By comparison, the water-soluble approach offers greater convenience, as its inner mold can be readily produced by using a 3D printer. The above method has been applied to soft robots and soft grippers, though it has yet to be widely adopted for soft exosuits, where the design process often still relies on trial-and-error or empirical experience [33,34].

Therefore, following the integrated casting methods, this paper presents the design and fabrication methodology for a soft pneumatic silicone exosuit intended for elbow rehabilitation. The main body of the exosuit is made of silicone and carbon fiber to ensure comfort and ease of movement. In the structure, a carbon fiber woven mesh replaces the traditional cloth fabric as the base plate, increasing structural stiffness to enable greater air chamber expansion under high pressure and thus a larger elbow bending angle. Additionally, the design of the air nozzle and its connection interface is refined to prevent leakage and simplify fabrication. In the silicone fabrication process, both PVA and PLA 3D-printed molds are used in the integrated casting method to enhance the airtightness performance of the exosuit. Moreover, instead of relying on trial-and-error approaches or empirical experience to determine chamber dimensions, the design process employs finite element simulation to systematically compare and optimize parameters such as the silicone hardness, chamber thickness, and the number of chambers under consistent pressure conditions. Finally, the experimental results show that the proposed exosuit achieves a maximum elbow flexion angle of 112 degrees at 1.5 bar and can achieve a 71-degree flexion under a load of 2 kg. When a PI controller was employed for elbow joint trajectory tracking, the maximum absolute error was limited to 4.29 degrees.

The contents of this paper are organized as follows: Section 2 proposes a brief introduction about the functionality, structure, and a novel integrated fabrication process of the soft pneumatic silicone exosuit. Section 3 describes some finite element simulations of the actuator, including the geometric parameters, hardness, and number of air chambers, which implies the optimization process of the proposed exosuit. To verify the performance of the prototype, bending and load capacity tests, together with wearable experiments using a dummy arm, are presented in Section 4 and the conclusion is proposed in Section 5.

https://doi.org/10.3390/act15060348

2. Materials and Methods

2.1. Structure Design

To illustrate the main structure, the prototype of the soft pneumatic silicone elbow exosuit consists of an actuator, a base plate, elastic bandages, an air tube, and an IMU (inertial measurement unit), as shown in Figure 1. It has been designed to conform to the human elbow biomechanic structure, thus helping the user with the elbow extension and flexion rehabilitation tasks. The actuator has overall dimensions of 320 mm × 100 mm × 28 mm (length × width × height, as shown in Figure 2) with a weight of 750 g. It is fabricated via silicone casting to satisfy the requirements of durability, flexibility, and airtightness. It consists of a series of air chambers connected in series by several airways. The first air chamber is connected to the air tube, allowing compressed air to be injected. The base plate is fabricated from a carbon fiber woven mesh and a silicone layer, with a total thickness of 3 mm. The elastic bandages, which pass through the through-holes on the front and rear sides of the actuator, serve as the physical human–robot interface to attach the exosuit onto the human forearm and upper arm. To facilitate wearing and positioning for users with different arm lengths, two rows of holes on the base plate of the exosuit are aligned with those on the carbon fiber woven mesh, and straps passed through the through-holes secure the exosuit, effectively preventing it from slipping off the arm during motion. When compressed air is injected into the actuator, the silicone air chambers generate an outward expansion force accompanied by obvious deformation. Since the greater stiffness of the carbon fiber woven mesh relative to the silicone constrains the actuator to bend in only one direction, due to the constraint of the elastic bandage, the expansion force is converted into a torque that is transmitted to the elbow joint of the user.

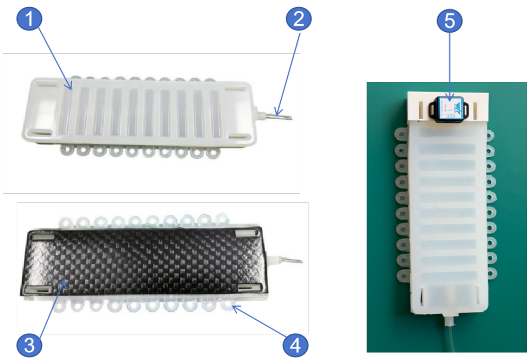

Figure 1. The prototype of soft pneumatic silicone elbow exosuit: The main components include: (**1**) the actuator, (**2**) the air tube, (**3**) the base plate, (**4**) the through-holes, and (**5**) the IMU resolution test.

To further improve airtightness, two changes were made in the design and fabrication of the air nozzle and connection, as shown in Figure 3. Before the silicone is molded, the air connection is pre-embedded near the airway inlet with a small gap left in place, which stops the PU tube from shifting inside the silicone layer during operation. A tapered locking groove is also pre-cast around the outer wall of the PU tube. After the tube is inserted into the pre-embedded connection, the joint is subjected to a secondary potting step. As a result, the PU tube becomes tightly bonded to the actuator, forming a reliable seal. This prevents the tube from moving or deforming during inflation/deflation and also protects it against external forces from the human elbow, thus avoiding air leakage at the interface between the connector and the surrounding silicone material.

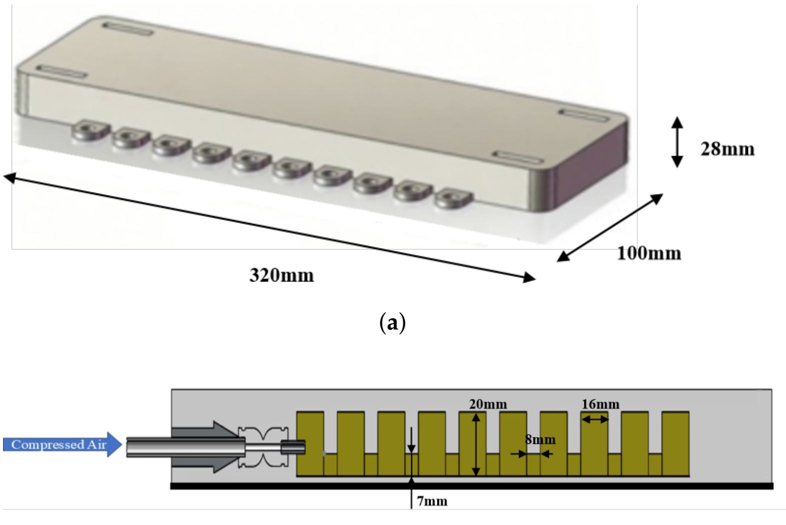

Figure 2. The structural design the soft pneumatic silicone elbow exosuit: (**a**) size; (**b**) section view.

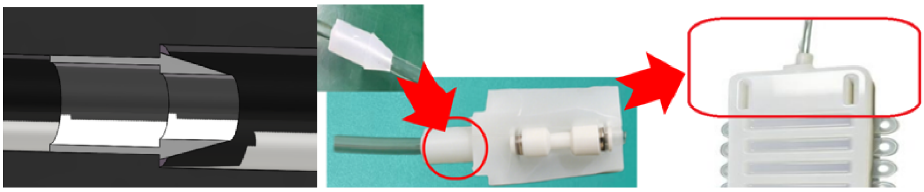

Figure 3. Structure of the air nozzle and the air connection: (**a**) a tapered locking groove of the air nozzle with a PU tube; (**b**) the air connection embedded in the actuator.

2.2. Fabrication Method

After preparing the 3D-printed molds of the air actuator, the fabrication process can be discussed. As illustrated in Figure 4, classical pneumatic actuators or soft robots made of silicone typically adopt a step-by-step casting process with split molds to form enclosed air chambers and airways. The outer mold is fabricated from 3D-printed materials (such as ABS and PLA, as shown in Figure 5) [20]. It is defined as a box-structured outer mold whose inner dimensions match the size of the air chambers. Inside the mold, the airway molds consist of separate molds for the air chambers and the airways, which are used to construct the enclosed structure. After mold closure, pouring the silicone mixture, and waiting about 1–2 h for curing and demolding, a silicone block with an open bottom (i.e., missing the bottom surface) is obtained. Subsequently, a bottom mold is used to invert the aforementioned silicone block to seal the bottom. However, due to the step-by-step casting process and the thin walls of the air chamber, the silicone adheres strongly to the PLA/ABS molds, making it difficult to detach. The external force applied during demolding can easily cause damage to the boundaries or induce local stress concentrations, thereby reducing the accuracy of motion and the service life of the actuator.

To address the above issues, this study proposes an integrated design method for the air chambers, as shown in Figure 6. Specifically, at the silicone pouring stage (originally in step 4), the inner mold, which consists of the air chamber and airway features, is printed integrally using a combination of water-soluble materials (such as PVA). This integrated printing ensures that all air chambers have consistent dimensions [35]. Meanwhile, the outer mold is still made of PLA to reduce processing cost and save 3D printing time. The inner PVA mold (in Figure 7) is used to form the air chamber, and the prototype is preliminarily fabricated using the casting method. The air chambers obtained by this sacrificial inner mold method exhibit better airtightness. The carbon fiber woven mesh serves as the base plate, replacing the thin cloth fiber layer used in the previous study [20]. This mesh is placed at the bottom of the PLA mold before silicone pouring and is then integrated into the prototype through secondary silicone casting. Subsequently, the prototype is placed in a 100 °C water bath for 10 h to dissolve the inner PVA mold, thereby eliminating the need for manual mechanical demolding. After the dissolution process, the liquefied PVA material is drained through the pre-designed airways and nozzle. The actuator is then dried in an oven at 60 °C for 2 h. Therefore, there is virtually no risk of air chamber breakage or stress concentration under normal operating conditions. The entire fabrication becomes seamless and damage-free, which improves the accuracy and consistency of the actuator. The carbon fiber woven mesh is used for reinforcement and directional expansion control. Moreover, the above base plate and the actuator are encapsulated as the exosuit using silicone of the same hardness, taking into account comfort when worn by humans.

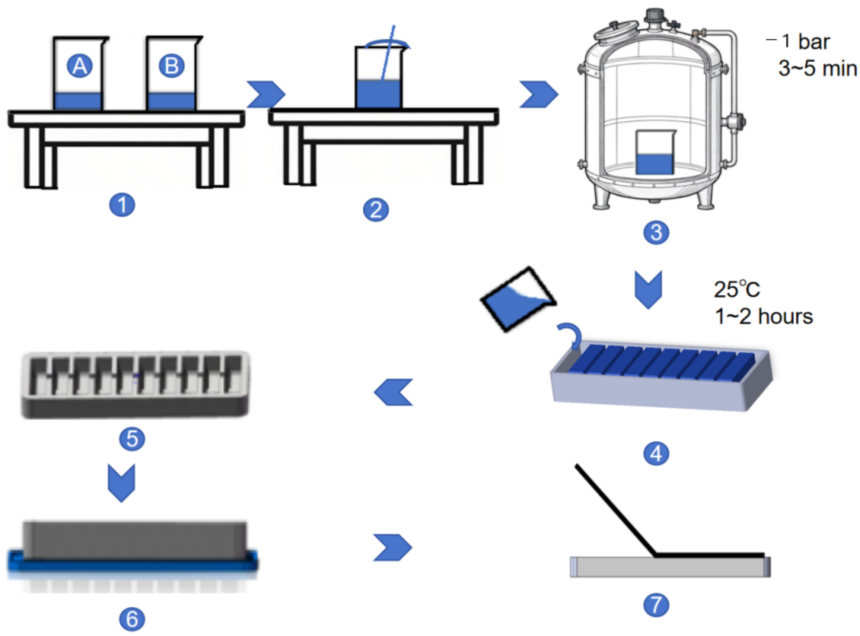

Figure 4. The classical pneumatic actuator fabrication process: the fabrication overview: (**1**) silicone preparation; (**2**) mixing and stirring; (**3**) degassing in a vacuum chamber; (**4**) silicone pouring; (**5**) curing and demolding; (**6**) bottom sealing; (**7**) carbon fiber woven mesh assembly. A and B represent the silicone base and curing agent, respectively.

Figure 5. The 3D-printed PLA mold.

https://doi.org/10.3390/act15060348

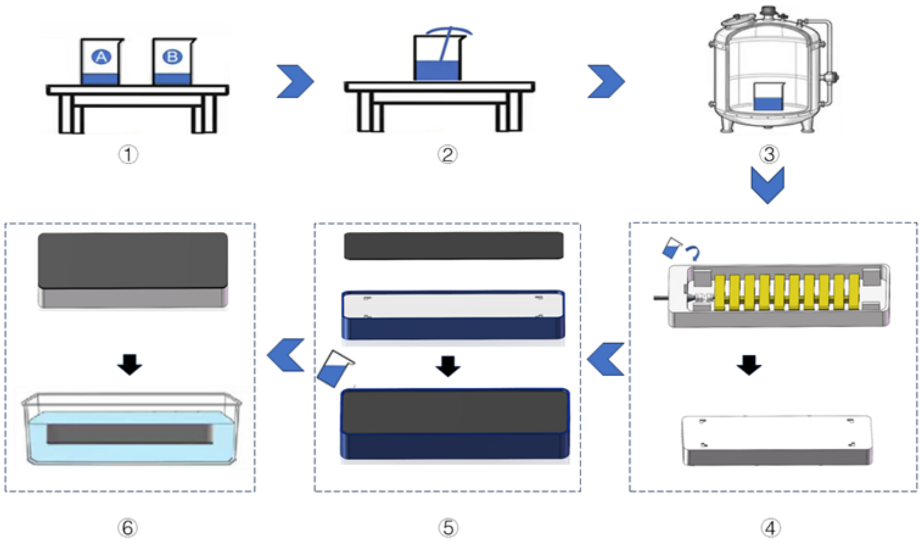

Figure 6. The proposed fabrication process: (**1**) silicone preparation; (**2**) mixing and stirring; (**3**) degassing in a vacuum chamber; (**4**) silicone pouring; (**5**) carbon fiber woven mesh assembly; (**6**) water bath and drying. A and B represent the silicone base and curing agent, respectively.

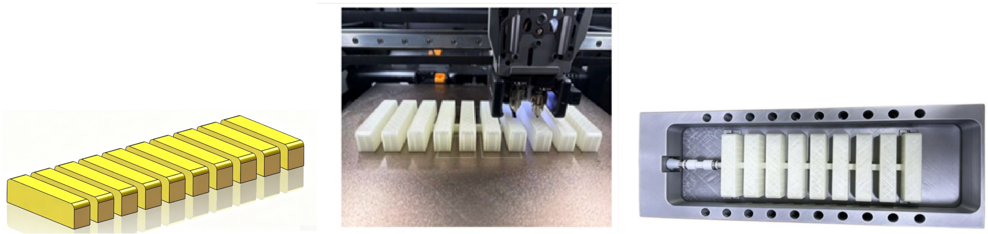

(**a**) (**b**) (**c**)

Figure 7. The proposed mold: (**a**) CAD drawing of inner molds and (**b**) 3D-printed PVA inner molds, and (**c**) assembly.

3. Finite Element Analysis and Optimization

In this study, the optimized dimensions of the exosuit are determined by the actuator bending deformation behavior based on the a-factor-at-a-time method. To this end, the stress–strain properties of silicone rubber tensile specimens with varying hardness are first discussed to provide the necessary material data for the finite element analysis simulations. Subsequently, the deformation behavior of the actuator is evaluated under different hardness levels, geometric dimensions, and numbers of air chambers, leading to the optimized actuator design.

3.1. Stress–Strain Characteristics of Silicone Tensile Specimens

To investigate the bending deformation behavior of the exosuit under pneumatic actuation and to optimize its actuator dimensions, tensile specimens of silicone rubber with varying hardness (Shore A hardness of 0, 10, 20, 25, 30 and 40) were required. The specimens were dumbbell-shaped as shown in Figure 8a. Their stress–strain relationships were obtained using the tensile testing platform shown in Figure 8b, and the experimental data were fitted with the Yeoh third-order hyper-elastic constitutive model (see Equation (1)). The results shown in Figure 8c were assigned to the silicone material model in the finite element analysis.

$$W = C_{10} \cdot (I_1 - 3) + C_{20} \cdot (I_1 - 3)^2 + C_{30} \cdot (I_1 - 3)^3 \quad (1)$$

where W is the strain energy density. C_{10}, C_{20}, and C_{30} denote the initial modulus under small strain, the softening/hardening behavior under moderate strain, and the degree of rapid hardening under large strain, respectively. These parameters are listed in Table 1. I_1 means the first principal invariant.

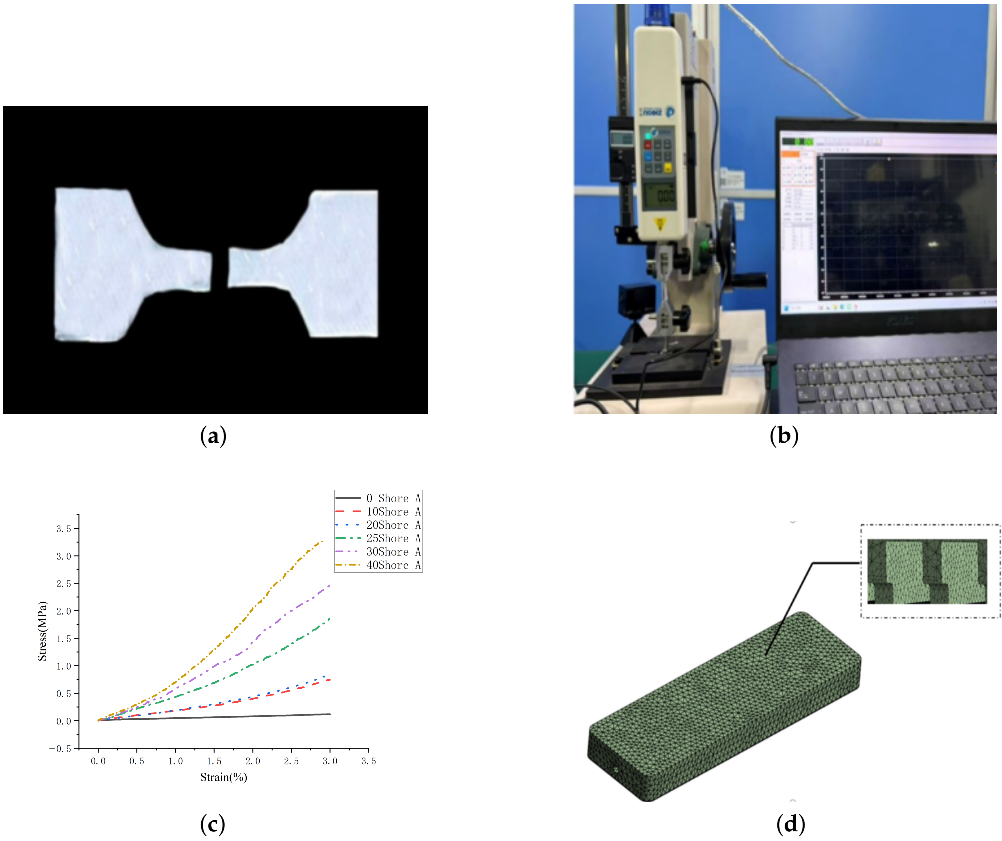

Figure 8. Material characterization and actuator modeling: (**a**) the dumbbell-shaped specimen; (**b**) experimental setups; (**c**) the curves of the relationship between the stress and strain; (**d**) the CAE model of the actuator.

Table 1. Parameters of the Yeoh third-order hyper-elastic constitutive model.

Hardness (Shore A)	C_{10}	C_{20}	C_{30}
0	499,330	−9081.7	256.9
10	24,560	1946.6	−10.338
20	77,784	3106	−17.702
25	100,330	6204.3	−60.143
30	88,686	7333.7	−93.991
40	120,130	22,061	−509.71

3.2. CAE Optimization of the Air Chamber

The 3D model of the actuator was imported into the finite element platform (ANSYS Workbench 2023R1) and multiple static simulations of the actuator inflation process were conducted. A parametric study was performed by iteratively modifying geometric parameters (actuator length, air chamber thickness, number of chambers) and the Shore hardness of silicone. To reduce computational cost, the carbon fiber braided mesh was simplified as a thin shell (Young's modulus: 230 GPa, Poisson's ratio: 0.301), bonded to the silicone body. Meshing was based on 3D solid elements. Tetrahedral elements were chosen for free meshing to accommodate complex geometries. Considering the near-incompressibility and large deformation of silicone, first-order fully integrated tetrahedral elements are prone to volumetric locking. Then, the model uses 10-node tetrahedral element SOLID187 (as shown in Figure 8d), which supports constitutive and large deformation analysis of hyper-elastic materials and has the ability to use displacement pressure (U-P) mixed formulas to handle large deformation problems of incompressible hyper-elastic materials.

During the contact definition, the top layer of the silicone actuator was set as the contact surface, and the carbon fiber reinforcement layer's surface was set as the target surface to improve the convergence efficiency of the contact calculation. Considering the hyper-elasticity of silicone and the large deformation during inflation, the Augmented Lagrangian method was employed to effectively suppress contact penetration under large deformation conditions, accommodating nonlinear problems while balancing accuracy and efficiency. Before the simulation, the proximal side attached to the upper arm was assigned a fully fixed constraint to simulate the rigid bonding between the exosuit and the upper arm. To model a smooth inflation process of the exosuit, six load steps were defined: the first five steps correspond to the pressure ramping stage, during which the internal cavity pressure increases linearly from its initial value of 0 bar with an increment of 0.3 bar per step, reaching 1.5 bar at the end of the fifth step. The upper pressure limit was conservatively set at 1.5 bar based on references [17,36]. The sixth load step is the pressure stabilization stage, maintaining a constant pressure of 1.5 bar. Each load step has a duration of 1 s. To quantitatively evaluate the degree of deformation of the structure, the amount of bending and the bending deformation ratio are selected as the core evaluation indicators. The bending amount d refers to the displacement value of each node relative to the initial position of the structure under stress (i.e., the higher the value, the more obvious the bending deformation). The bending deformation ratio is defined as the ratio of the maximum bending displacement to the initial length of the structure L_0.

$$\eta = \frac{d}{L_0} \times 100\% \tag{2}$$

First of all, analyzing the impact of silicone hardness allows the determination of the optimal Shore hardness for the elbow exosuit actuator (in Figure 9). In this simulation, let L_0 = 320 mm , which is selected to adequately accommodate the upper-limb dimensions of adult males aged from 18 to 60 years (i.e., GB/T10000-1988, human dimensions of Chinese adults [37]). When the silicone hardness approaches 0 Shore A, under an air pressure of 1.5 bar, the maximum bending amount d of the actuator is only 83.29 mm, with a deformation ratio L_0 of 26.03%. This is attributed to the excessively low cross-linking density of the silicone molecular chains at extremely low hardness, resulting in high viscosity and low elasticity. When the hardness increases to 10 Shore A, under the same pressure, d rises to 224.39 mm and L_0 reaches 70.12%. This indicates that with a moderate increase in hardness, the elastic restoring force of the material is enhanced, and the actuation deformation gradually transitions from localized expansion at extremely low hardness to coordinated global bending along the chamber axis. When the hardness increases further to 20 Shore A, d rises to 300.51 mm and L_0 reaches 93.91%, at which point the high-strain region covers most of the chamber area. At 25 Shore A, the maximum amount of bending reaches 390.38 mm, with a deformation ratio of 121.99%. However, when the hardness increases to 30 Shore A, the maximum bending amount decreases to 361.22 mm and the deformation ratio drops to 112.88%. This demonstrates that as the silicone hardness increases, the elastic modulus rises, significantly enhancing the actuator's resistance to deformation, while the structural morphological change during inflation becomes suppressed. When the hardness is further increased to 40 Shore A, the maximum bending amount is reduced to 243.51 mm and the deformation ratio to 76.10%, further confirming the above trend. In summary, the optimal hardness is determined to be 25 Shore A.

https://doi.org/10.3390/act15060348

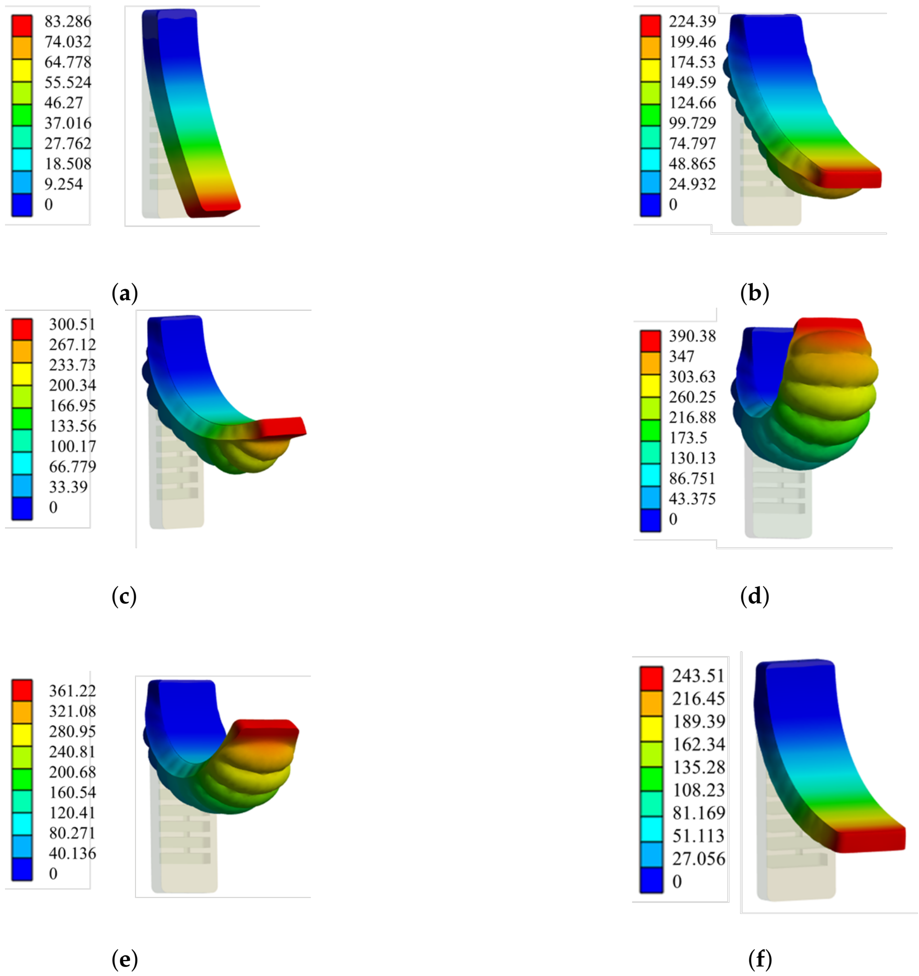

Figure 9. Finite element analysis results: hardness of the silicone material (bending deformation unit: mm). (**a**) 0 Shore A; (**b**) 10 Shore A; (**c**) 20 Shore A; (**d**) 25 Shore A; (**e**) 30 Shore A; (**f**) 40 Shore A. The unit in the figure is mm.

Then, based on the determination of 25 Shore A silicone as the actuator material, the length L_0 was further optimized. As shown in Figure 10, when L_0 is set to 310 mm, 320 mm, 330 mm, and 340 mm, the corresponding maximum bending amounts d are 385.49 mm, 390.38 mm, 389.13 mm, and 377.10 mm, respectively; the corresponding maximum deformation ratios η are 120.47%, 121.99%, 121.60%, and 117.84%, respectively. Based on the above results, L_0 = 320 mm is considered optimal. Then, to optimize the thickness of the actuator, the air chamber thickness was set to 14 mm, 16 mm, and 18 mm for finite element simulation. From the results shown in Figure 11, the corresponding maximum bending amounts d are 248.19 mm, 390.38 mm, and 372.38 mm, respectively. Meanwhile, the corresponding maximum deformation ratios η are 77.56%, 121.99%, and 116.37%, respectively.

After the above optimization process, the regulation of the number of air chambers on bending performance was investigated as follows (in Figure 12). The finite element analysis was performed on actuators with nine, 10, and 11 air chambers to obtain the final optimized structural dimensions. The results are shown in Figure 10. For the actuator with nine air chambers, d was 380.75 mm (η = 118.98%). The overall structural stiffness was relatively high, indicating a strong ability to resist bending deformation. For the actuator with 10 air chambers, d reached 390.38 mm (η = 121.99%). The increased number of air chambers enabled a more uniform transmission path of the bending load within the structure. When the number of air chambers was increased to 11, d was 343.48 mm (η = 107.34%).

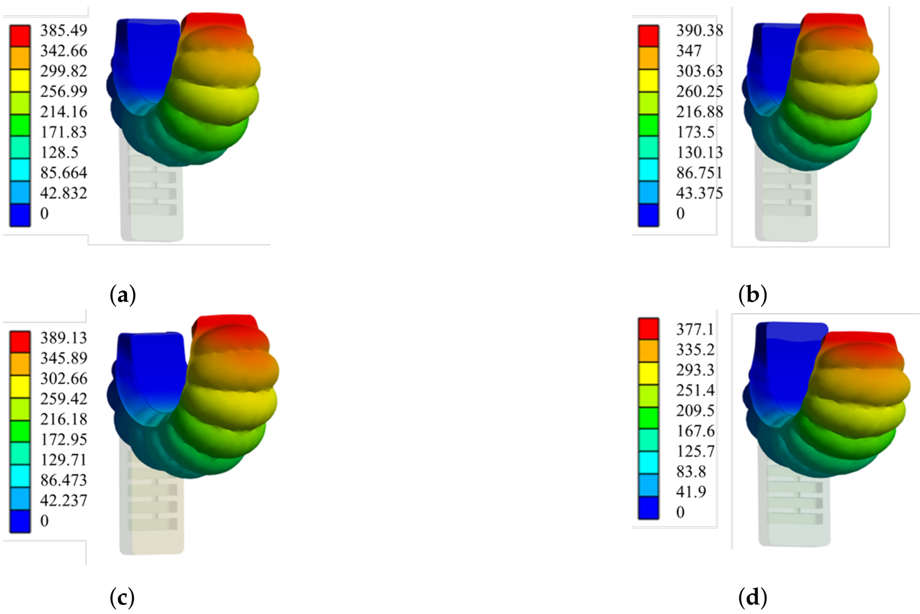

Figure 10. Finite element analysis results: length of the actuator. (**a**) 310 mm; (**b**) 320 mm; (**c**) 330 mm; (**d**) 340 mm.

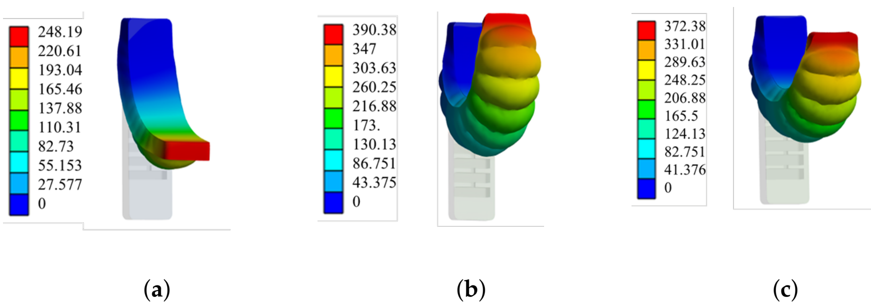

Figure 11. Finite element analysis results: number of the air chambers: (**a**) 14 mm; (**b**) 16 mm; (**c**) 18 mm. The unit in the figure is mm.

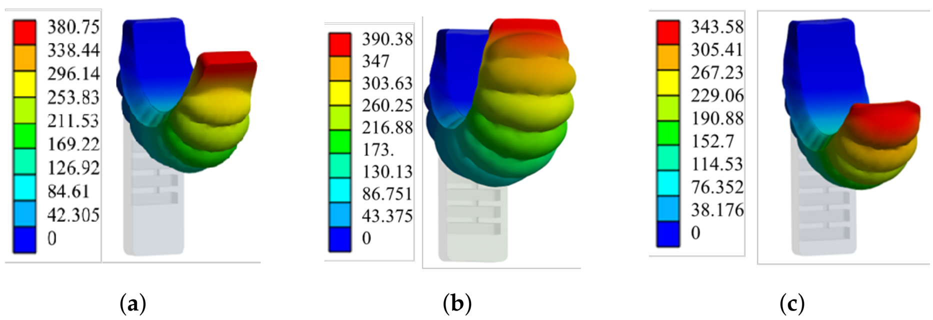

Figure 12. Finite element analysis results: number of the air chambers: (**a**) 9; (**b**) 10; (**c**) 11. The unit in the figure is mm.

4. Experiments and Results

4.1. Experimental Setup

In this subsection, the performance of the proposed prototype of the soft pneumatic silicone exosuit was tested through the experimental setups displayed in Figure 13. Compressed gas was provided by an air compressor and kept at a constant pressure via a pressure regulator. For the valve control, the PWM signal derived from the PC was directed to an Arduino board, and the PWM module then transmitted it to two high-speed valves (MHE2, Festo Inc., Esslingen, Germany) at an operating frequency of 100 Hz. Both valves are 3/2-way solenoid valves, separately controlling air intake and exhaust. When the first intake valve opens and the second exhaust valve closes, the compressed air enters the actuator, and the exosuit flexes the elbow; when both valves are closed, the actuator holds its position; when the first intake valve closes and second exhaust valve opens, the actuator exhausts air, and the exosuit returns to its initial position by gravity. For sensing, one IMU (WT61PC, Witmotion Inc., Beijing, China) was employed to record the elbow joint position of the exosuit.

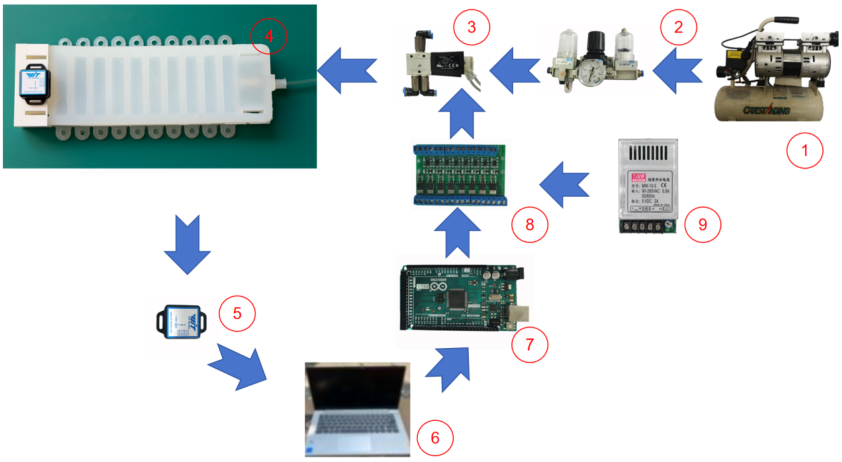

Figure 13. Experiment setups: 1—air compersssor; 2—pressure regulator; 3—high-speed valve; 4—the prototype of the exosuit; 5—IMU; 6—PC; 7—Arduino 2560; 8—PWM module; 9—DC module.

In the bending and load capacity experiment, one side of the exosuit was mounted onto a metal bracket using a vise located on the top of the bracket. The weights were secured by the bandage on the other side of the exosuit. During the experiment, these standard weights served as the load, and a PC sent commands to control the high-speed valve for the pneumatic actuator inflation, causing the exosuit to bend, while the IMU recorded its maximum deformation angle. In another experiment, the exosuit was installed on a silicone manikin arm and fixed to the same metal bracket, serving as a substitute for a human subject to avoid safety and ethical concerns in rehabilitation experiments. Therefore, the proposed exosuit employed a silicone pneumatic actuator to produce repeated elbow flexion and extension, simulating passive rehabilitation training through valve-controlled inflation and deflation.

4.2. Experiment Process A: Bending and Load Capacity Testing of the Exosuit

From the above-mentioned, a bearing and load capacity test of the proposed exosuit was performed, in which weights of 0 g, 500 g, 1 kg, and 2 kg were suspended from the soft exosuit while it was secured with bandages, as shown in Figure 14a. The maximum deformation angle of the exosuit was recorded as shown in Figure 14b, with the following experimental details: The PC sent an inflation signal to the Arduino 2560 and the PWM module, causing the first intake valve state to open and the second exhaust valve state to close. Then, after waiting 10 s for the exosuit inflation process, the two high-speed valves both closed to keep the exosuit on station, and the maximum air pressure was limited to 1.5 bar for safety. Additionally, the previous study of a similar exosuit system (X. Gao [17]) was also recorded for comparison.

https://doi.org/10.3390/act15060348

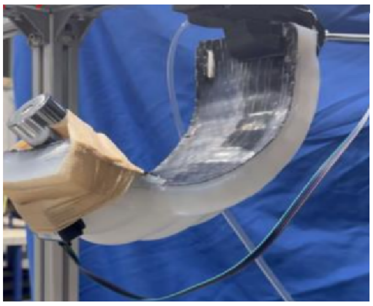

(a)

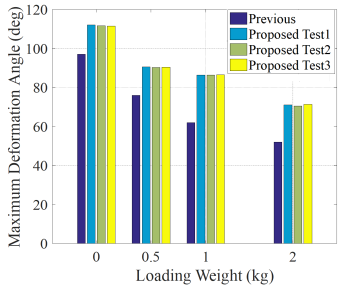

(b)

Figure 14. Bending and load capacity testing: (**a**) the experiment process and (**b**) results.

All the measurements were recorded three times in the experiment, and the average values were calculated for the discussion. From the results, the maximum deformation angle of the proposed exosuit in average equals 112 deg, 90 deg, 86 deg and 71 deg for 0 kg, 0.5 kg, 1 kg, and 2 kg in the loading condition, respectively, which are all obviously improved from the previous study (with the improvement rates of 15.46%, 18.42%, 38.71%, and 36.54%, respectively). These benefits are attributed to improvements in the fabrication process, particularly the integrated design and fabrication of the silicone actuator and the base layer of the carbon fiber woven mesh. Statistical analysis (paired *t*-test) revealed that the improvements in maximum deformation angles under all loading conditions were significant ($p = 0.004 < 0.05$).

4.3. Experiment Process B: Elbow Joint Passive Rehabilitation Task

To simulate the task of the proposed exosuit assisting a stroke wearer in passive elbow rehabilitation training, a manikin elbow flexion/extension trajectory was set as a sinusoidal signal with a period of 20 s and an amplitude of 20 degrees in Equation (3), which can make a smooth motion process of the exosuit. It should be mentioned that the trajectory amplitude employed in our experiments is consistent with the clinical requirements for stroke survivors within the first 4 weeks of elbow rehabilitation, but it does not match the activities of daily living (ADL) [38]. The typical PI position control method was implemented for the tracking trajectory controller in the experiment. It ran on a PC and was programmed using Simulink Real-Time (MATLAB 2016b, MathWorks, Inc., Natick, MA, USA), and the system achieved an execution rate of 1 kHz. As illustrated in Figure 13, the proposed exosuit was set onto a silicone manikin arm to mimic a human subject to avoid safety risks and ethical issues.

$$\theta_d = 20\sin\left(0.2\pi t - \frac{\pi}{2}\right) + 20\ \text{deg} \tag{3}$$

The PI controller parameters are determined using the Ziegler–Nichols tuning method, yielding P = 2.5 and I = 0.008. Since the actuator is driven by high-speed on/off valves, the Arduino maps the PI control law output (x) to a PWM duty cycle (y) using the conversion function y = 75x/64, where y > 0 corresponds to charging (admitting high-pressure air into the exosuit) and y < 0 corresponds to discharging (releasing air from the exosuit). The tracking position and the tracking error ($e = \theta - \theta_d$) are recorded in Figure 15. The maximum absolute tracking error of the PI controllers equals 4.29 degrees. The root mean square of the tracking error equals 2.89 degrees. The above results indicate that the proposed PI controller can be effectively used in the joint angular trajectory tracking control. Meanwhile, these results confirmed that the proposed control method is better than the comparative studies of the soft elbow exosuit system (e.g., 5.18 degrees of the maximum absolute error in [39]), and similar tracking performance in other soft wearable robots (e.g., 0.045 rad of the maximum absolute error in the PAM exoskeleton [40] and 4.85 degrees of the mean absolute error in the motion capture glove in [35]), which also proves that the proposed exosuit has the potential ability to be used in rehabilitation training tasks for stoke patients. Moreover, the experimental results also indicate that the peak of tracking error is prone to occur in the extreme position of the flexion–extension motion, which is due to the nonlinear hysteresis characteristics of the soft pneumatic actuators.

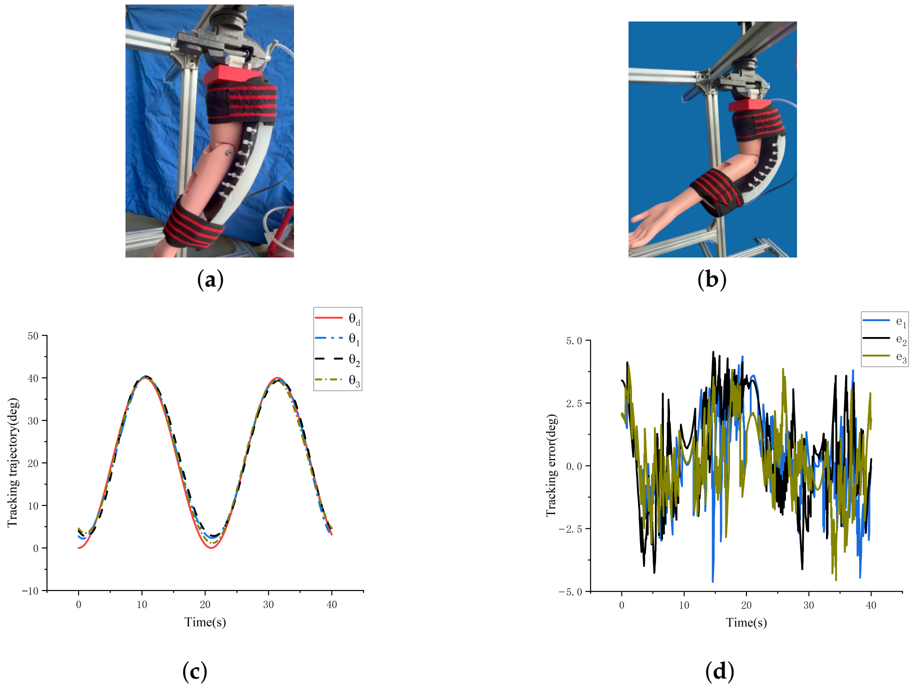

Figure 15. Elbow joint passive rehabilitation task: (**a**) the initial joint position; (**b**) the maximum joint position; (**c**) angular position trajectory; (**d**) tracking error.

Moreover, during the experiments, three flexible contact force sensors (FSR DF9-40, ChengTEC, Shanghai, China, as shown in Figure 16) were installed: one between the elastic bandage and the forearm of the manikin arm, one between the actuator and the elbow joint, and one between the bandage and the upper arm, to measure the contact pressure between the exosuit and the wearer. The test results indicate that the human–robot contact pressure at the forearm is the largest, with a peak value of up to 13.73 N, followed by that at the elbow joint, peaking at 7.61 N, while that at the upper arm is the smallest, peaking at 3.73 N. This difference is because the bandage located at the upper arm mainly serves to fix the exosuit during elbow flexion, whereas the bandage located at the forearm is mainly used for the bending part of the silicone actuator. It frequently contacts the wearer and provides assistive force. The elbow joint also experiences considerable contact due to its proximity to the actuator's bending region.

However, it should be noted that the above exosuit driven by the silicone actuator is still at an exploratory stage regarding its control methods, perception capabilities, and fabrication techniques. The exosuit prototype has not yet been tested on human subjects. With further testing, we intend to explore the feasibility of its engineering and clinical applications, including: (1) the dynamic model and high-precision control methods for the proposed soft elbow exosuit; (2) integration with flexible sensor meshes and other flexible electronics toward a smart rehabilitation exosuit; (3) energy-saving solutions, such as alternative energy harvesting from the actuator; and (4) production cost considerations and the potential for mass assembly line manufacturing [41,42].

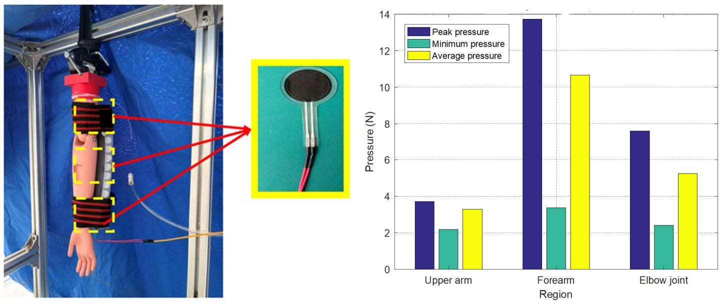

(**a**) (**b**)

Figure 16. Pressure measurements on upper arm, forearm, and elbow joint: (**a**) FSR and (**b**) experimental data.

5. Conclusions

In this study, a novel soft pneumatic silicone exosuit was described to assist with flexion and extension of the human elbow, and its design and fabrication method were illustrated. The proposed exosuit is activated by several silicone-made air chambers. It can bend about 112 degrees without any load and 71 degrees with a load of 2 kg from the experiments. Meanwhile, combined with the PI controller, the maximum absolute error of the angular tracking trajectory was limited to 4.29 degrees. This performance is attributed to the use of the integrated fabrication method with a 3D-printed PVA mold, to the combination of the carbon fiber woven mesh of the base plate with the air chamber, and to the finite element analysis of the geometric parameters, hardness, and number of air chambers in the structural design. Therefore, the proposed exosuit shows great potential for practical rehabilitation tasks.

Author Contributions: Conceptualization, Z.Z., D.D., X.H., C.X. and L.H.; methodology, Z.Z., D.D. and X.H.; software, D.D. and X.H.; validation, Z.Z., D.D. and X.H.; formal analysis, D.D. and X.H.; investigation, Z.Z., C.X. and X.Z.; resources, Z.Z.; data curation, D.D.; writing—original draft preparation, Z.Z.; writing—review and editing, Z.Z., D.D., X.H., C.X., X.Z. and D.S.; visualization, Z.Z.; supervision, Z.Z., D.D., X.H., C.X., X.Z., L.H. and H.G.; project administration, D.S., X.Z., L.H. and H.G.; funding acquisition, Z.Z. and L.H. All authors have read and agreed to the published version of the manuscript.

Funding: The National Natural Science Foundation of China (grant number 62303330); the Department of Education of Liaoning Province (grant number JYTQN2023072); and the Natural Science Foundation of Liaoning Province of China (grant number 2024-BS-159).

Institutional Review Board Statement: The study was conducted in accordance with the Declaration of Helsinki, and approved by the Northeastern University Bioethics Committee for Biology and Medicine (NEU-EC-2021B017S).

Informed Consent Statement: Informed consent was obtained from all subjects involved in the study.

Data Availability Statement: Data is contained within the article.

Acknowledgments: The authors thank Xingfeng Gao and Xing Li for their helpful advice and comments on this study.

Conflicts of Interest: The authors declare no conflicts of interest.

Abbreviations

The following abbreviations are used in this manuscript:

PAM	Pneumatic Artificial Muscle
3D	Three-Dimensional
PLA	Polylatide
ABS	Acrylonitrile Butadiene Styrene
PVA	Polyvinyl Alcohol
PI	Proportional–Integral
ADL	Activities of Daily Living

References

1. Gao, S.; Chen, J.; Xia, Y.; Li, X.; Ma, W.; Yang, H.; Li, J.; Zhou, X.; Jia, T.; Xu, Y.; et al. Wearable technologies for assisted mobility in the real world. *Nat. Commun.* **2025**, *16*, 10988.
2. Ganesh, G.S.; Khan, A.R.; Khan, A. A qualitative study on rehabilitation services at rural rehabilitation practice in Uttar Pradesh, India: Insights from rehabilitation professionals in low-resource contexts. *Work* **2024**, *35*, 10519815251337729.
3. Ertl, M.; Gurtner, L.M. Human sciences can increase technology acceptance in rehabilitation science: A call for action. *Front. Rehabil. Sci.* **2024**, *5*, 1356445.
4. Chen, C.; Chen, T.; Zhao, N.; Dong, S. Regional maldistribution of humanresources of rehabilitation institutions in China Mainland based on spatial analysis. *Front. Public Health* **2022**, *10*, 1028235.
5. Jesus, T.S.; Landry, M.D.; Hoenig, H.; Dussault, G.; Koh, G.C.; Fronteira, I. Is Physical Rehabilitation Need Associated with the Rehabilitation Workforce Supply? An Ecological Study Across 35 High-Income Countries. *Int. J. Health Policy Manag.* **2020**, *11*, 434.
6. Mashud, G.; Hasan, S.K.; Alam, N. Advances in Control Techniques for Rehabilitation Exoskeleton Robots: A Systematic Review. *Actuators* **2025**, *14*, 108.
7. Yang, C.J.; Zhang, J.F.; Chen, Y.; Dong, Y.M.; Zhang, Y. A review of exoskeleton-type systems and their key technologies. *Proc. Inst. Mech. Eng. Part C J. Mech. Eng. Sci.* **2008**, *222*, 1599–1612.
8. Lo, H.S.; Xie, S.Q. Exoskeleton robots for upper-limb rehabilitation: State of the art and future prospects. *Med. Eng. Phys.* **2012**, *34*, 261–268.
9. Tu, X.; Xuan, Z.; Li, J.; Chen, S.; He, J. Iterative learning control applied to a hybrid rehabilitation exoskeleton system powered by PAM and FES. *Clust. Comput.* **2017**, *20*, 2855–2868.
10. Wu, X.; Li, Z.; Kan, Z.; Gao, H. Reference Trajectory Reshaping Optimization and Control of Robotic Exoskeletons for Human-Robot Co-Manipulation. *IEEE Trans. Cybern.* **2020**, *50*, 3740–3751.
11. Talley, C.; Young, V.; Thompson, W.; Grann, A.; Sawicki, G.; Tekes, A. A Bio-Inspired Assistive Exoskeleton for Supporting Shoulder and Daily Activities. *J. Eng. Sci. Med. Diagn. Ther.* **2026**, *9*, 0210041.
12. Copaci, D.; Arias, J.; Moreno, L.; Blanco, D. Shape memory alloy (SMA)-based exoskeletons for upper limb rehabilitation. In *Rehabilitation of the Human Bone-Muscle System*; Intechopen: London, UK, 2022.
13. Cheng, C.; Dai, W.; Wu, T.; Chen, X.; Wu, M.; Yu, J.; Jiang, J.; Lu, H. Efficient and Precise Homo-Hetero Teleoperation Based on an Optimized Upper Limb Exoskeleton. *IEEE/ASME Trans. Mechatron.* **2024**, *30*, 3722–3734.
14. Zimmermann, Y.; Forino, A.; Riener, R.; Hutter, M. ANYexo: A versatile and dynamic upper-limb rehabilitation robot. *IEEE Robot. Autom. Lett.* **2019**, *4*, 3649–3656.
15. Zimmermann, Y.; Sommerhalder, M.; Wolf, P.; Riener, R.; Hutter, M. ANYexo 2.0: A fully actuated upper-limb exoskeleton for manipulation and joint-oriented training in all stages of rehabilitation. *IEEE Trans. Robot.* **2023**, *39*, 2131–2150.
16. Knill, A.S.; Studer, B.; Wolf, P.; Riener, R.; Goffredo, M.; Maggioni, S. Kinematic Assessment of Upper Limb Movements Using the ArmeoPower Robotic Exoskeleton. *IEEE Trans. Neural Syst. Rehabil. Eng.* **2024**, *32*, 3942–3952.
17. Gao, X.; Sun, Y.; Hao, L.; Yang, H.; Chen, Y.; Xiang, C. A new soft pneumatic elbow pad for joint assistance with application to smart campus. *IEEE Access* **2018**, *6*, 38967–38976.
18. Hou, X.; Zeng, X.; Zhao, Z.; Liu, G.; Shan, D.; Xu, J. Structure Design and Manufacturing Method of the Silicon-Based Elbow Exoskeleton. In *Proceedings of the 2025 WRC Symposium on Advanced Robotics and Automation (WRC SARA), Beijing, China, 10 August 2025*; IEEE: Piscataway, NJ, USA, 2025; pp. 101–106.
19. Ismail, R.; Ariyanto, M.; Perkasa, I.A.; Adirianto, R.; Putri, F.T.; Glowacz, A.; Caesarendra, W. Soft elbow exoskeleton for upper limb assistance incorporating dual motor-tendon actuator. *Electronics* **2019**, *8*, 1184.
20. Li, N.; Yang, T.; Yu, P.; Chang, J.; Zhao, L.; Zhao, X.; Liu, L. Bio-inspired upper limb soft exoskeleton to reduce stroke-induced complications. *Bioinspirat. Biomimet.* **2018**, *13*, 066001.

21. Yang, M.; Wu, J.; Jiang, W.; Hu, X.; Iqbal, M.I.; Sun, F. Bioinspired and hierarchically textile-structured soft actuators for healthcare wearables. *Adv. Funct. Mater.* **2023**, *5*, 2210351.
22. Xing, L.; Wang, M.; Zhang, J.; Chen, X.; Ye, X. A survey on flexible exoskeleton robot. In *Proceedings of the 2020 IEEE 4th Information Technology, Networking, Electronic and Automation Control Conference (ITNEC), Chongqing, China, 12–14 June 2020*; IEEE: Piscataway, NJ, USA, 2020; pp. 170–174.
23. Ramos, O.; Múnera, M.; Moazen, M.; Wurdemann, H.; Cifuentes, C.A. Assessment of soft actuators for hand exoskeletons: Pleated textile actuators and fiber-reinforced silicone actuators. *Front. Bioeng. Biotechnol.* **2022**, *10*, 924888.
24. Chiaradia, D.; Xiloyannis, M.; Antuvan, C.W.; Frisoli, A.; Masia, L. Design and Embedded Control of a Soft Elbow Exosuit. In *Proceedings of the 2018 IEEE International Conference on Soft Robotics (RoboSoft), Livorno, Italy, 24–28 April 2018*; IEEE: Piscataway, NJ, USA, 2018; pp. 565–571.
25. Yirmibesoglu, O.D. Direct 3D printing of silicone elastomer soft robots and their performance comparison with molded counterparts. In *Proceedings of the 2018 IEEE International Conference on Soft Robotics (RoboSoft), Livorno, Italy, 24–28 April 2018*; IEEE: Piscataway, NJ, USA, 2018; pp. 295–302.
26. Wang, Y.; Gregory, C.; Minor, M.A. Improving mechanical properties of molded silicone rubber for soft robotics through fabric compositing. *Soft Robot.* **2018**, *5*, 272–290.
27. Sridhar, E.P.; Erel, V.; Nasirian, A.; Wijesundara, M.B. Design, development, and evaluation of a pneumatically actuated soft wearable robotic elbow exoskeleton for reducing muscle activity and perceived workload. *J. Rehabil. Assist. Technol. Eng.* **2025**, *12*, 20556683251347517.
28. Zhao, Z.R.; Xia, C.; Zeng, X.Y.; Hou, X.Y.; Hao, L.N.; Shan, D.X.; Xu, J.Q. Design of a PEBA–Silicone Composite Magneto-Sensitive Airbag Sensor for Simultaneous Contact Force and Motion Detection. *Sensors* **2025**, *25*, 5823.
29. Tse, Y.A.; Liu, S.; Yang, Y.; Wang, M.Y. A Flexible Connector for Soft Modular Robots Based on Micropatterned Intersurface Jamming. In *Proceedings of the 2020 3rd IEEE International Conference on Soft Robotics (RoboSoft), New Haven, CT, USA, 15 May–15 July 2020*; IEEE: Piscataway, NJ, USA, 2020; pp. 150–155.
30. Sridar, S.; Nguyen, P.H.; Zhu, M.; Lam, Q.P.; Polygerinos, P. Development of a soft-inflatable exosuit for knee rehabilitation. In *Proceedings of the 2017 IEEE/RSJ International Conference on Intelligent Robots and Systems (IROS), Vancouver, BC, Canada, 24–28 September 2017*; IEEE: Piscataway, NJ, USA, 2017; pp. 3722–3727.
31. Schumacher, C.M.; Loepfe, M.; Fuhrer, R. 3D printed lost-wax casted soft silicone monoblocks enable heart-inspired pumping by internal combustion. *Rsc Adv.* **2014**, *4*, 16039–16042.
32. Silva, A.; Fonseca, D.; Neto, D.M.; Babcinschi, M.; Neto, P. Integrated design and fabrication of pneumatic soft robot actuators in a single casting step. *Cyborg Bionic Syst.* **2024**, *5*, 0137.
33. Merdan, O. Fabrication and thermo-mechanical evaluation of a polyurethane-based porous structure intended for use in robotic gripping applications. *Eng. Sci. Technol.* **2025**, *70*, 102170.
34. Gamus, B.; Salem, L.; Ben-Haim, E.; Gat, A.D.; Or, Y. Interaction Between Inertia, Viscosity, and Elasticity in Soft Robotic Actuator With Fluidic Network. *IEEE Trans. Robot.* **2017**, *34*, 81–90.
35. Hosie, O.; Isaksson, M.; McCormick, J.; Tirosh, O.; Hensman, C. The Design and Validation of an Open-Palm Data Glove for Precision Finger and Wrist Tracking. *Sensors* **2025**, *25*, 367.
36. Abdulrab, H.Q.; Mohd, N.; Muhammad, R.; Faudzi, A. Snake-like soft robot using 2-chambers actuator. *Elektr. J. Electr. Eng.* **2018**, *17*, 34–40.
37. *GB/T 10000-1988*; Human Dimensions of Chinese Adults. Standardization Administration of China (SAC): Beijing, China, 1988.
38. Morrey, B.F.; Askew, L.J.; Chao, E.Y. A biomechanical study of normal functional elbow motion. *J. Bone Jt. Surg.* **1981**, *63*, 872–877.
39. Wu, Q.; Wang, Z.; Chen, Y. sEMG-Based Adaptive Cooperative Multi-Mode Control of a Soft Elbow Exoskeleton Using Neural Network Compensation. *IEEE Trans. Neural Syst. Rehabil. Eng.* **2023**, *31*, 3384–3396.
40. Zhao, Z.R.; Hao, L.N.; Liu, M.F.; Gao, H.Z.; Li, X. Prescribed performance model-free adaptive terminal sliding mode control for the pneumatic artificial muscles elbow exoskeleton. *J. Mech. Sci. Technol.* **2021**, *35*, 3183–3197.
41. Zhang, W.; Merces, L.; Ma, J.; Becker, C.; Karnaushenko, D.; Tang, H.; Qu, J.; Ferro, L.M.M.; Huang, Y.; Yan, Y.; et al. A bioinspired microdevice unifying energy storage and actuation through hydration control. *Nat. Commun.* **2026**, *17*, 2650.
42. Merces, L.; Ferro, L.M.M.; Thomas, A.; Karnaushenko, D.D.; Luo, Y.; Egunov, A.I.; Zhang, W.; Bandari, V.K.; Lee, Y.; McCaskill, J.S.; et al. Bio-Inspired Dynamically Morphing Microelectronics toward High-Density Energy Applications and Intelligent Biomedical Implants. *Adv. Mater.* **2024**, *36*, 2313327.

https://doi.org/10.3390/act15060348